Mitigating self-discharge and improving the performance of Mg–S battery in $Mg[B(hfip)_4]_2$ electrolyte with a protective interlayer†

Dasari Bosubabu, *[a] Zhenyou Li, [a] Zhen Meng, [a] Li Ping Wang,[a] Maximilian Fichtner *[ab] and Zhirong Zhao Karger *[ab]

Magnesium sulfur (Mg S) battery is receiving much research attention because of its high theoretical energy density, low-cost and sustainable electrode materials. However, the major issues such as self-discharge, low sulfur utilization in cathode and magnesium anode passivation severely hamper the battery operation. In this study, spontaneous magnesium polysulfide formation is observed in the Mg $[B(hfip)_4]_2$, $Mg(TFSI)_2$ $MgCl_2$ electrolytes, which leads to severe self-discharge of Mg S cells. Interestingly, unlike in lithium sulfur battery, these magnesium polysulfides forms as crystalline magnesium polysulfide on the magnesium foil, which could escalate the self-discharge of the cells. The incorporation of graphene polyaniline coated carbon cloth (GPN PANI@CC) as a protective interlayer which effectively adsorbs the polysulfide and inhibit the self-discharge of Mg S cells in the non-corrosive $Mg[B(hfip)_4]_2$ electrolyte. This interlayer not only improve the polysulfide retention in cathode but also the capacity values in $Mg[B(hfip)_4]_2$ electrolyte compared to $Mg(TFSI)_2$ $MgCl_2$ electrolyte. The cells with interlayer show the initial capacity of 1121 mA h g ^{1} and maintained a capacity of 500 mA h g ^{1} after 150 cycles with coulombic efficiency of >99%. This cell design strategy provides a promising approach for improving metal sulfur batteries.

Introduction

The worldwide demand for advanced rechargeable batteries with higher energy density, lower cost and longer lifespan is continuously growing to meet the requirements for global e-mobility and grid-scale electricity storage.[1,2] With the perspectives of the high energy density and low cost, metal–sulfur batteries are stimulating tremendous research interests.[3–5] Besides lithium–sulfur (Li–S) battery, multivalent metal–sulfur systems such as magnesium–sulfur (Mg–S), calcium–sulfur (Ca–S) and aluminum–sulfur (Al–S) batteries are emerging as promising post-lithium technologies.[6–11] In the quest for a suitable metal anode for sulfur-based batteries, Mg represents an attractive candidate in terms of the high volumetric capacity (*e.g.* 3833 mA h cm^{-3} for Mg *vs.* 2205 mA h cm^{-3} for Li), ample availability in earth crust (~13.9% Mg compared to ~0.0007% of Li) and good safety (less dendrite formation and less reactive at ambient conditions).[12–15] Hence forth, an electrochemical couple of a magnesium anode with a sulfur cathode exhibits a high theoretical energy density (1722 W h kg^{-1} and 3200 W h L^{-1}), which could result in a high-energy and economical battery system.[16–19] Compared to the intensive research and progress made for Li–S batteries, the research of the Mg–S system is still in an early stage of R&D.[18,20–22] Large efforts have been devoted to discovering a sulfur compatible electrolyte with favorable electrochemical and chemical properties.[23–26] The electrolytes are based on different chemical combinations such as $Mg(HMDS)_2$–$AlCl_3$ (HMDS = hexamethyldisilazide) and $Mg(TFSI)_2$–$MgCl_2$ (TFSI = bis(trifluoro methanesulfonyl)imide) have been initially utilized for Mg–S batteries due to their chemical compatibility with sulfur.[27–31] Recently developed chloride-free Mg-ion conductive salts represent new generation non-corrosive and efficient electrolytes.[32–37] In particular, highly reversible sulfur redox mechanism and discharge/charge chemistry have been demonstrated by using the magnesium tetrakis(hexafluoroisopropyloxy)borate $Mg[B(hfip)_4]_2$ (hfip = $OC(H)(CF_3)_2$) electrolytes.[38–40]

Nevertheless, the Mg–S battery is still facing critical fundamental issues, including (i) rapid self-discharge (ii) passivation of Mg anode due to the dissolved sulfur species in the electrolyte (iii) inferior conversion rate for recharging the cell due to the ionically and electronically insulating nature of sulfur and MgS.[37,41] In particular, a foremost challenge that needs to be addressed is the serious self-discharge behavior of the Mg–S

[a]*Helmholtz Institute Ulm (HIU) Electrochemical Energy Storage, Helmholtzstraße 11, Ulm D 89081, Germany*

[b]*Institute of Nanotechnology, Karlsruhe Institute of Technology (KIT), Hermann von, Helmholtz Platz 1, Eggenstein Leopoldshafen, D 76344, Germany. E mail: zhirong. zhao karger@kit.edu; bosu.dasari@kit.edu; m.fichtner@kit.edu*

† Electronic supplementary information (ESI) available. See DOI: 10.1039/d1ta06114c

batteries, where Mg can react with the dissolved sulfur in the electrolyte forming soluble magnesium polysulfides without applying any external circuit.[30] Richter *et al.* have compared the self-discharge behavior of both Li–S and Mg–S batteries *via* computational studies and suggested that the rate of self-discharge in the Mg–S system is much higher than in the Li–S system.[42] Most recently, Ford *et al.* experimentally examined the self-discharge phenomena with various electrolytes and unveiled that the Mg–S cells severely suffered from self-discharge in the $Mg(TFSI)_2$–$MgCl_2$ electrolyte, losing up to 96% of the capacity in the first cycle after a certain open circuit potential (OCP) hold period.[43] These results manifest that there is an imperative need to address the self-discharge problem for enhancing the performance of Mg–S batteries.[44]

To control the self-discharge behavior, various approaches could be adopted concerning the matured similar Li–S system.[45] Integration of an interlayer has shown many beneficial properties for mitigating the polysulfide shuttle effect, such as (i) acting as an upper current collector to facilitate electron transport and high active material utilization; (ii) as a filter to intercept/absorb the migrating polysulfides and thereby suppress the polysulfide diffusion; (iii) reutilizing the trapped active materials and stabilizing the active materials in the cathode compartment.[46 48] Very recently, it has been demonstrated that the functionalized separator or interlayer can significantly improve both capacity retention and coulombic efficiency for Mg–S batteries using the $Mg[B(hfip)_4]_2$ electrolytes.[49,50] However, no focused attention has been paid to the self-discharge behavior in these studies. Herein, the self-discharge behavior of the Mg–S cells in the $Mg[B(hfip)_4]_2$ (denoted as MBR) electrolytes has been extensively investigated. Furthermore, interlayer strategies have been developed towards the inhibition of the self-discharge of the Mg–S cells. Among the various studied cells, graphene (GPN)–polyaniline (PANI) @carbon cloth (CC) interlayer cell exhibits less self-discharge and high capacity retention. Besides, GPN–PANI coating can suppress the polysulfide diffusion and reactivate the non-conductive active material inside the cathode compartment. As a result, the self-discharge can be minimized and the reversible capacity of the cells can be improved. In addition, the electrochemical performance of the Mg–S cells was also compared in $Mg[B(hfip)_4]_2$ and $Mg(TFSI)_2$–$MgCl_2$ based electrolytes.

Experimental section

Preparation of S@GPN–PANI composite and the cathode

20 mg of graphene nanoplatelets (Sigma Aldrich), 20 mg of polyaniline (Emerald) (Sigma Aldrich) were mixed in 50 ml of dimethylformamide (DMF) (A), and the solution was sonicated for 2 h. Similarly, 60 mg of sulfur was dispersed in 50 ml of DMF under sonication (B). Solution (C) contained 5 mg polyvinylpyrrolidone (PVP) in 1000 ml deionized water. When (A) + (B) was transferred into (C), the solution turned immediately from colorless to a white color indicating colloidal sulfur formation. Unlike orthorhombic sulfur, this colloidal sulfur was hydrophilic which disperse evenly in water and the PVP in the water covers the surface of colloidal sulfur and the carbon composite. This mixture was stirred overnight until the colloidal sulfur was adsorbed by the carbon. The formed composite (S@GPN–PANI) was filtered by vacuum filtration and dried at 60 °C for 12 h.[48,51 54] 95 wt% of S@GPN–PANI was mixed with an additional 5 wt% PVP binder in water. The slurry was coated on a lightweight activated carbon cloth and dried overnight at 70 °C. The sulfur loading is 1 mg cm^{-2} of the electrode. The electrode was used as the cathode in the Mg–S cells.

Fabrication of GPN–PANI@CC interlayer

Initially, 45 mg of GPN and 45 mg of PANI were added in 25 ml of dimethylformamide (DMF) individually in two beakers and ultra-sonicated for 60 minutes. Both the solutions were mixed and stirred together for an hour. This composite solution was diluted with water followed by vacuum filtration, and the filtrate was dried overnight at 80 °C to obtain the dry GPN–PANI composite. Subsequently, 90 mg of GPN–PANI composite was mixed with 10 mg of PVP in an aqueous solution and coated on a carbon cloth by drop-casting. Finally, the coated carbon cloth was dried at 80 °C. The concentration of binder and GPN–PANI solution was optimized to obtain a thin coating ($\sim$1 mg cm^{-2}).

Electrolyte preparation

Magnesium hexafluoroisopropyl borate salt ($Mg[B(hfip)_4]_2$) was synthesized according to our previous reports.[38] 0.4 M Mg $[B(hfip)_4]_2$ electrolyte was prepared by dissolving some amount of the salt into a proper amount of DME and used as the chloride-free electrolyte. 0.4 M $Mg(TFSI)_2$ in 0.4 M $MgCl_2$ was mixed in a proper amount of DME and used as a chloride-containing $Mg(TFSI)_2$–$MgCl_2$ electrolyte. The magnesium polysulfide (Mg_xS_y) was prepared by placing 50 mg of sulfur powder and Mg foil in a vial along with in 2 ml electrolyte, the solution is aged for 10 days. The yellow supernatant was collected and used as the Mg_xS_y solution.

Mg–S cell assembly and electrochemical measurements

The aforementioned S@GPN–PANI electrode was used for the cathode. The interlayer was placed above the cathode. The glass fiber filter paper (GF/C Whatman) was used as a separator soaked with 100 μl chloride-free non-nucleophilic 0.4 M Mg $[B(hfip)_4]_2$/DME or chloride containing 0.4 M $Mg(TFSI)_2$–$MgCl_2$ in DME, respectively. The inert top layer on the Mg foil was removed with the help of a knife inside the glovebox and used as the anode. The 2032 type coin cells were fabricated inside the glovebox (MBRAUN) with the H_2O < 0.1 ppm and O_2 level of <0.1 ppm.

Galvanostatic charge–discharge measurements and symmetric cell measurements were conducted using an electrochemical workstation (ARBIN Instruments). The Mg–S cells were cycled between 0.5–2.5 V and 0.3–2.4 V *vs.* Mg^{2+}/Mg in 0.4 M MBR electrolyte and 0.4 M $Mg(TFSI)_2$–$MgCl_2$ electrolyte at room temperature, respectively. The OCV, CV, and EIS tests were performed using a Biologic VMP3 potentiostat.

Structural characterization

The Bruker D8 advance powder X-ray diffractometer with a Cu Kα source was used for conducting X-ray diffraction (XRD) analysis. Scanning electron microscopy (SEM) and energy-dispersive X-ray spectroscopy (EDX) were performed in a Zeiss LEO 1530 with EDX detector X-max N from Oxford instruments. Absorption spectra were collected using a Cary 5000 UV-Vis-NIR spectrophotometer. BET analysis was done by using the micromeritics ASAP 2020 instrument.

Results and discussion

Graphene–polyaniline based sulfur composite and interlayer

The graphene–polyaniline based sulfur composite (denoted as S@GPN–PANI) with a high sulfur content of 60% was prepared by the ultrasonic dispersion method.[51,52,55] The surface morphologies of the composites were examined by field emission scanning electron microscopy (FE-SEM) as depicted in Fig. 1. The graphene exhibits a two-dimensional sheet-like structure with multiple lamellar layers Fig. 1a, and the pristine PANI comprises the polymer particles that are agglomerated and cross-linked Fig. 1b and c reveals that the GPN–PANI composite has a sponge-like structure, in which the PANI is enclosed, together with the crumpled graphene sheets. After sulfur incorporation, the structural integrity of the composite was maintained Fig. 1d. The elemental mapping of the S@GPN–PANI sample indicates a homogeneous distribution of nitrogen, and sulfur throughout the carbon sample (Fig. 1f–h).

The surface and porous properties of the composites and the individual components were analyzed by N_2 physisorption Fig. S1.† Compared to the graphene with a specific surface area of 783 $m^2\ g^{-1}$, the GPN–PANI composite still maintains a moderate surface area of 298 $m^2\ g^{-1}$, indicating the fairly uniform distribution of the PANI on the surface of the graphene. After the sulfur incorporation, most of the voids in the GPN–PANI composite host were filled, resulting in a low surface area (34 $m^2\ g^{-1}$) and reduced pore volume (0.117 $cm^3\ g^{-1}$) for the S@GPN–PANI composite. The XRD patterns of GPN and GPN–PANI composite show two broad diffraction peaks at $2\theta = 27°$, 43° corresponding to (002), (101) planes of the hexagonal graphitic carbon Fig. S2.† The composite S@GPN–PANI exhibits dominant sulfur reflections, implying some amount of sulfur is located on the surface of the carbon. The Raman spectra of the S@GPN–PANI composite shows that the graphitic feature represented with the G-band at 1592 cm^{-1} was retained while the intensity of the D-band at 1350 cm^{-1} notably decreased due to the lattice defects/distortions Fig. S3.† The missing vibration stretching bands at 1246 cm^{-1} for the C–N bonds of the benzenoid rings of PANI could be ascribed to the strong adsorption of sulfur.

The functional interlayer was fabricated by casting the GPN–PANI composite mixed with PVP (10%) in an aqueous solution on the activated carbon cloth (CC). The mass loading of the composite is approximately 1 mg cm^{-2}, and the thickness of the interlayer is 1.224 mm (Fig. S4†).

Self-discharge in Mg–S cell

As mentioned earlier, the rate of self-discharge of the Mg–S batteries can be extremely high, depending on the used electrolytes.[43] This demands meticulous attention to control this problem for enhancing the battery performance. The self-discharge in Mg–S cells should be induced by the internal chemical reactions between sulfur and Mg. In this work, these reactions were first examined by simply mixing some amount of sulfur powder and a piece of polished Mg foil in the solutions of $Mg[B(hfip)_4]_2$ (denoted as MBR) and $Mg(TFSI)_2$–$MgCl_2$ in

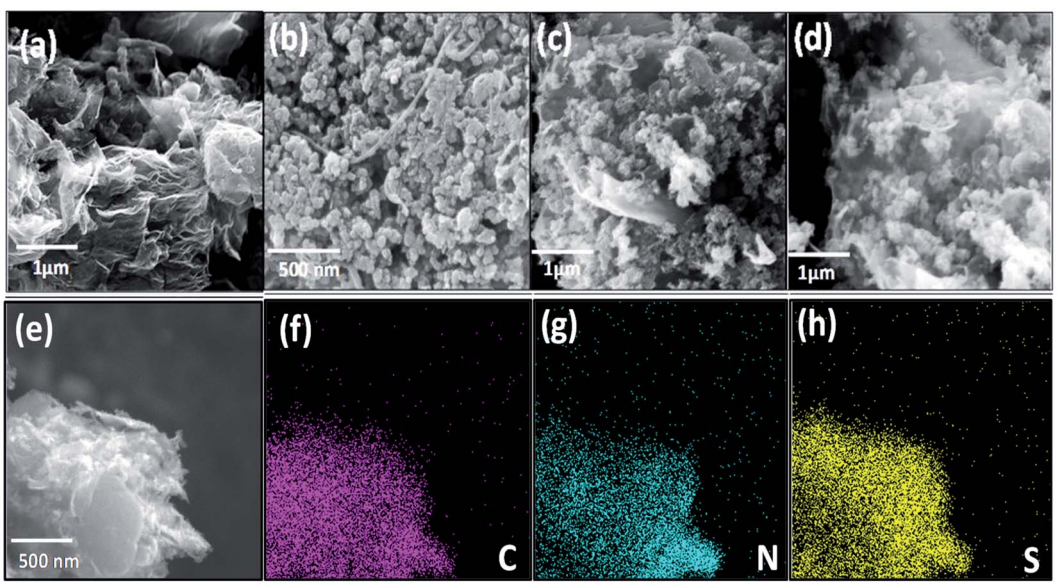

Fig. 1 FE-SEM images of (a) GPN (b) PANI (c) GPN PANI (d) S@GPN PANI (e h) elemental mapping of carbon, nitrogen, and sulfur in S@GPN PANI.

dimethoxymethane (DME), respectively. Fig. 2 displays the digital photographs of spontaneous polysulfide formation during the aging periods. The colorless fresh MBR electrolyte turned yellow after the 24 h rest period, indicating the spontaneous polysulfide formation in the electrolyte. After 10 days of aging, impressively, most of the sulfur had dissolved in the electrolyte and dark yellow solids at the bottom of the glass bottle appeared. This demonstration indicates that magnesium polysulfides can be spontaneously converted from soluble species to insoluble precipitates in the electrolyte. The formation of solid magnesium polysulfide (Mg_3S_8) has been identified in other studies on Mg–S batteries.[56] For confirmation, a similar test was also conducted with sulfur and MBR electrolyte without Mg foil where no noticeable color change, *i.e.* polysulfide formation was not observed even after 10 days of the resting period Fig. S5.† This verifies that the Mg metal can react with dissolved sulfur and forming magnesium polysulfide. Even when sulfur has relatively low solubility in ethereal solvents (~10 mM saturated in DME),[57] the thermodynamically favored formation of the highly soluble polysulfide can spontaneously proceed and drive the sulfur continually to dissolve into the electrolyte and further react with the Mg. Similar results were also observed with the $Mg(TFSI)_2$–$MgCl_2$ electrolyte Fig. S6.† However, in MBR electrolyte solid Mg_xS_y crystals grown as a needle-like structure whereas polyhedrons were observed in the $Mg(TFSI)_2$–$MgCl_2$ solution Fig. S7.† Hence, these experiments suggest that in a real cell, the active sulfur material could dissolve into the electrolyte and react with the Mg anode during the rest period, if it is not well restrained within the cathode compartment and diffuse to the anode side. Subsequently, the cell befalls severe self-discharge followed by reduction of capacity.

Further, UV/Vis spectra were recorded to analyze the spontaneously formed sulfur species in the electrolyte. In an Ar-filled glove box, a quartz glass cuvette was filled with 2 ml of MBR electrolyte along with 50 mg of sulfur, and a polished Mg foil was submerged. The electrolyte to sulfur ratio was 40 μl per mg of sulfur to mimic the real Mg–S cell conditions. The color change after 24 h is shown in Fig. 2g and h. The dissolved polysulfide species were monitored by recording UV/Vis spectra over a holding time from 1 to 168 h. As depicted in Fig. 2i, the 1 h spectra display the peaks at 280 and 370 nm which represent S_8 and S_6^{2-} species, respectively.[58] This indicates a rapid initiation of the spontaneous formation of Mg polysulfide when Mg is in contact with the sulfur molecules in the solution. After 2 hours, the absorption intensities were amplified and the peak shifted from 280 to 292 nm, along with peak broadening at 370 nm. After 24 h, the width and height of the absorption

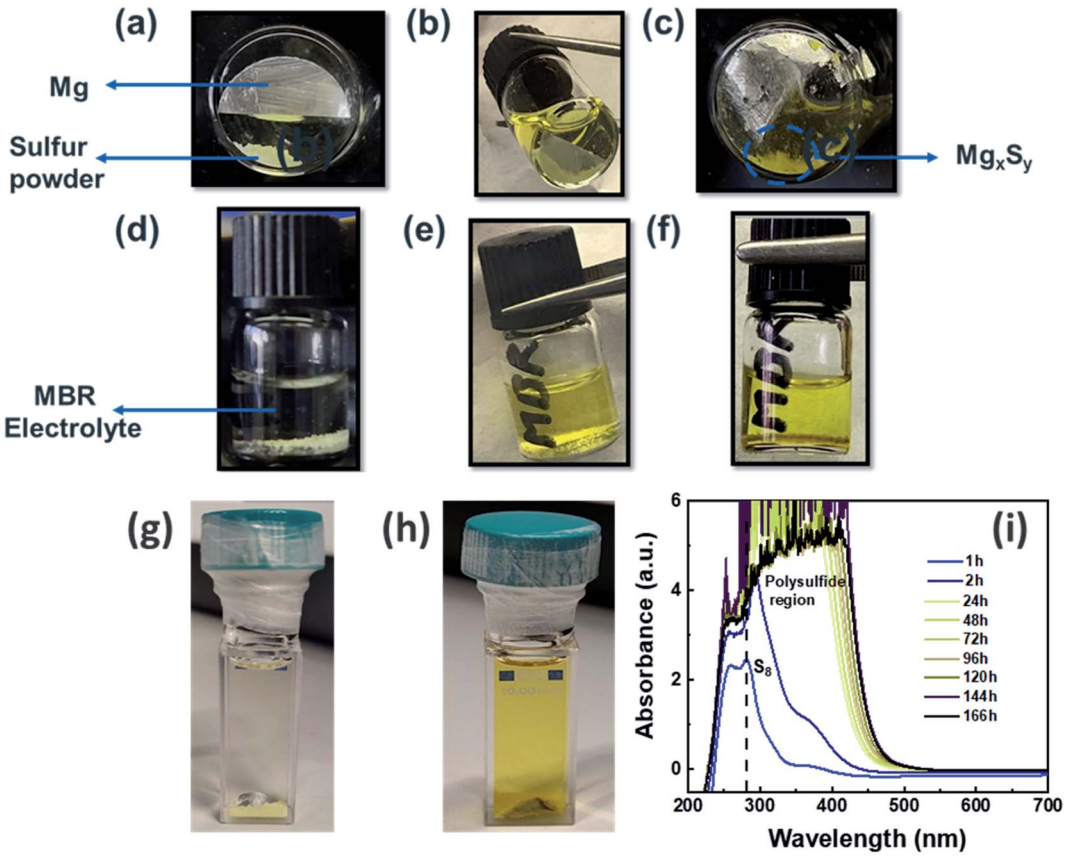

Fig. 2 Digital photos indicating the polysulfide formation in MBR electrolyte: (a and d) fresh, (b and e) after 24 h, (c and f) after 10 days; quartz glass cuvette containing sulfur powder, Mg foil, and MBR electrolyte: (g) fresh, (h) after 24 h, (i) respective UV/Vis spectra in various holding periods.

bands were considerably enlarged and beyond the measuring range due to the significantly increased concentration of the polysulfides. Despite the limitation of these measurements for identifying the individual sulfide species, the merged broad absorption band in the range from 230–450 nm recorded after 24 h could imply that the high-order Mg polysulfides undergo a spontaneous transformation and disproportionate reactions forming various polysulfide species.[58,59]

In addition, the influence of these polysulfides on electrolyte performance was also investigated. Symmetric cells with the configuration of Mg‖electrolyte‖Mg and similar cells with 0.1 M of Mg_xS_y in the MBR electrolyte were fabricated. The symmetric cells were subjected to Mg plating/stripping at a current density of 1 mA cm^{-2} for a time duration of 700 h. In the case of Mg‖electrolyte‖Mg cell, the stripping/plating proceeded smoothly as reported in the literature.[38] While the cell with Mg_xS_y additive showed higher stripping/plating voltages, and this polarization behavior was maintained over the cycling period Fig. S8.† This could be caused by the Mg_xS_y shuttle effect and the passivation of the Mg surface, which can increase the interfacial resistance of the cell. This confirms the detrimental effect of Mg_xS_y on the electrolyte properties.

Electrochemical studies

The interlayer strategy has been employed to minimize the self-discharge of the Mg–S cell in this study. Using the S@GPN–PANI cathode, Mg anode and MBR electrolyte, three cell configurations were constructed *i.e.* the pristine cell (no interlayer) and the cell with an additional CC or GPN–PANI@CC interlayer, respectively. The static electrochemical stability of these batteries was monitored *via* the voltage drop with the rest time as shown in Fig. 3. The open-circuit voltages (OCV) of three cells were measured to be between 2.16 ± 0.015 V immediately after the cell assembly. Irrespective of the configuration, all the cells showed a decrease in the voltage indicating the polysulfide formation *via* an internal chemical reaction. These higher-order Mg_xS_y species could dissolve and diffuse into the ether electrolyte. As a result, the OCV of batteries decreases slowly with time. After 10 days of rest, the OCV of the cells with CC, GPN–PANI@CC interlayers was 1.89 V and 1.98 V, respectively, which was higher than that of cells without interlayer (1.83 V) as shown in Fig. 3a. This increment of OCV implies that the coating of GPN–PANI on carbon cloth served as an excellent self-discharge inhibitor for the Mg–S batteries. Electrochemical impedance spectra (EIS) were conducted to analyze the changes of the cell before and after the OCV test Fig. 3b. Initially, the pristine cell showed low impedance but after the OCV test, the impedance of the cell was drastically increased, which might be caused by the passivating layer on the electrode surface. Irrespective of the cell configuration this behavior is similar Fig. S9.† Moreover, after 10 days of a rest period, the pristine, GPN–PANI@CC interlayer cells were investigated by galvanostatic cycling as shown in Fig. 3c. The pristine cell delivered a poor initial capacity of 70 mA h g^{-1}, displaying a higher overpotential, which could be due to the severe polysulfide dissolution in the electrolyte and passive layer on the electrodes. Interestingly, a gradual increase in capacity with the cycle number has been perceived, implying that the dissolved

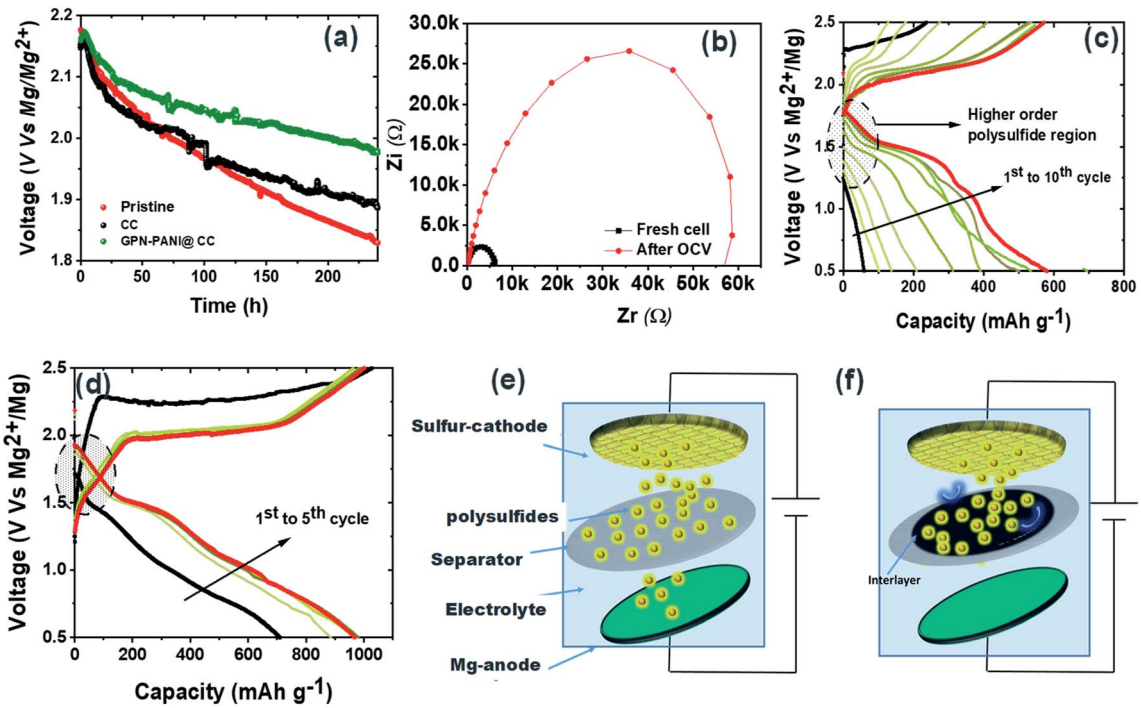

Fig. 3 (a) OCV test on pristine, CC interlayer, and GPN PANI@CC interlayer cells (b) impedance of pristine cell fresh after OCV (c and d) after OCV test, charge discharge profiles of pristine, GPN PANI@CC interlayer cells (e and f) schematic representation of polysulfide control in the pristine and GPN PANI@CC interlayer cells.

polysulfides (active cathode material) can be reactivated in the cell. In the initial cycle, no capacity was observed in the voltage range above 1.5 V (this might be a higher-order polysulfide region). When the cycle number increased, the sloping plateau gradually appeared in the voltage range of 1.75 to 1.5 V. After 10 cycles, the cell reached its maximum capacity of 600 mA h g^{-1} Fig. 3c. The improvement in capacity was ~8.5 times to that of the initial cycles. It is worth mentioning that the capacity recovery observed in this study could be attributed to the utility of the carbon cloth for both the sulfur cathode and interlayer, which acts as an adsorbent of the dissolved sulfur species.

However, analogous to the above pristine cell, the GPN–PANI@CC interlayer cell also suffered the initial high polarization and poor coulombic efficiency as shown in Fig. 3d. It could be ascribed to the parasitic reactions of polysulfides on the Mg metal, which consume more energy during charge. After the initial cycle, the coulombic efficiencies tended to increase and reached 98%, which could again hint at the recovery of the dissolved polysulfide. Notably, the GPN–PANI@CC interlayer cells exhibited a much higher initial capacity of ~700 mA h g^{-1} and an increase in capacity to a value of 983 mA h g^{-1} after 3 cycles. These results indicate that in the interlayer cell only a small quantity of the polysulfide was present in the electrolyte compared to the pristine cell and it could be recovered within a few cycles. More importantly, this cell configuration greatly improved the Mg_xS_y retention capability, also enabled the re-utilization of trapped active material in the conductive interlayer. Hence, the GPN–PANI@CC interlayer acts as a good anti-self-discharge configuration. To further understand, the self-discharge test of pristine and GPN–PANI@CC interlayer cells after 5 charge–discharge cycles are carried out (Fig. S10†). The pristine, GPN–PANI@CC interlayer cells are cycled for 5 charge–discharge cycles after that cells are rested for about 72 h. In both the cells higher potential capacity loss is observed at early stage of 6^{th} cycle discharge, which might indicates the polysulfide dissolution in the electrolyte. In case of pristine cell the 6^{th} cycle discharge capacity shows huge capacity decay around 238 mA h g^{-1} indicates poor polysulfide absorption. However, most of the capacity is regained in the consecutive cycle. Whereas in GPN–PANI@CC interlayer cell less capacity decay (39 mA h g^{-1}) is observed, interestingly all the capacity is retained back in the next cycle. This indicates interlayer cells shows high self discharge ability than pristine cell. Fig. 3e and f illustrate the potential advantage of the GPN–PANI@CC interlayer to control the polysulfide diffusion.

The galvanostatic charge–discharge cycling of pristine, CC, GPN–PANI@CC interlayer cells was investigated at 0.1C between the voltage range of 0.5 to 2.5 V *vs.* Mg/Mg^{2+} in 0.4 M MBR electrolyte with an OCV period of 15 min, respectively (Fig. 4a–c). All the cells show nearly the same potential hysteresis (ΔE) *i.e.* ~0.5 V. Interestingly, in the case of the GPN–PANI@CC interlayer cell, the polarization (ΔE) decreased to 0.353 V upon cycling, which indicates that the CC interlayer coated with GPN–PANI can effectively enhance the electronic conductivity of the sulfur composite. However, all the cells show nearly similar charge–discharge plateaus in the initial cycle. Notably, three plateaus were observed during the discharge process. The upper voltage plateau at 1.85–1.5 V might represent the conversion of sulfur to higher-order polysulfide, which is highly soluble in an electrolyte and has rapid formation

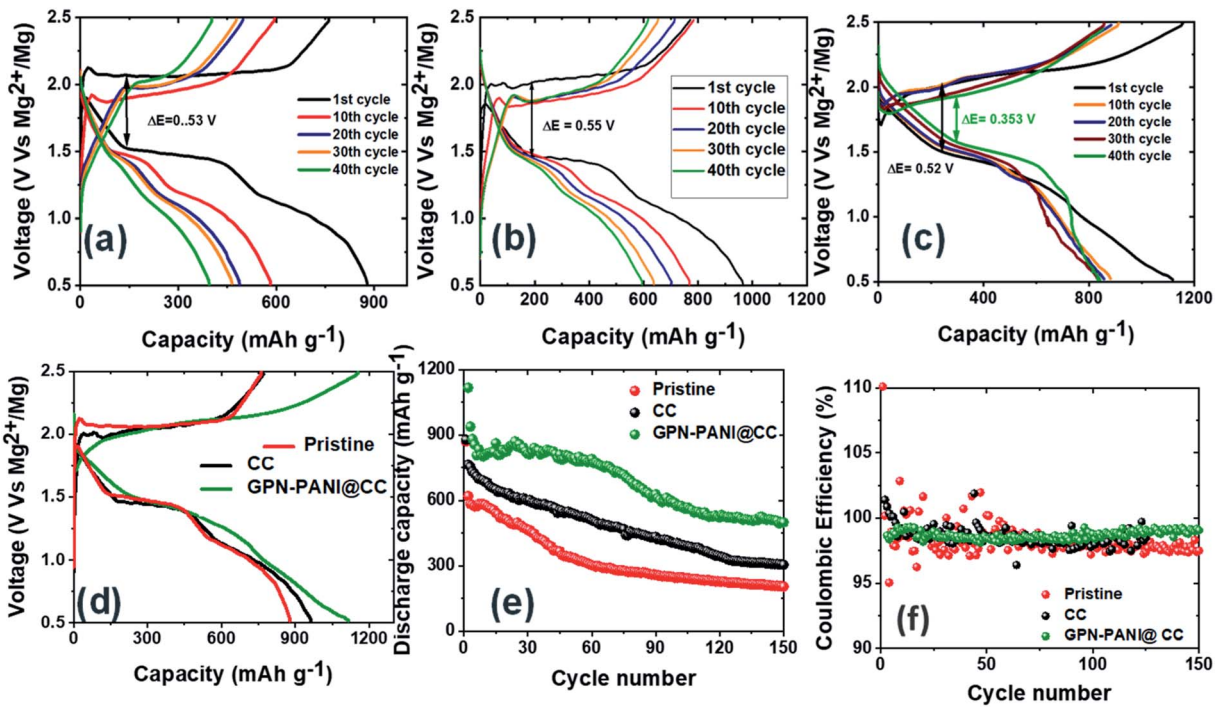

Fig. 4 (a c) Charge discharge cycling curves (d) comparison of initial cycles (e) capacity *vs.* cycle number plot (f) coulombic efficiency of pristine, CC, GPN PANI@CC interlayer cells.

kinetics. The other two sloping plateaus at 1.5–1.4 V and 1.17–0.5 V are the conversion of lower-order insoluble polysulfides to MgS_2 and MgS. However, the charging process displays one plateau at ~2 V which should be the oxidation of MgS to sulfur *via* polysulfide intermediate. Particularly, interlayer cells showed stable upper discharge plateau (>1.5 V) over 40 cycles, which may be attributed to the polar surface of the GPN–PANI coating that can anchor the active material and enable redox reactions. Fig. 4d shows the comparison of charge–discharge curves of pristine, CC, GPN–PANI@CC cells. Notably, at the initial charge of the pristine cell, a sudden voltage spikes up to 2.12 V was seen whereas 2.0 V (CC interlayer) and 1.8 V (GPN–PANI@CC interlayer) were observed for other cells. This may indicate that the discharge product of the cathode in the pristine cell needs activation energy owing to its poor conductivity. The interlayer cells displayed a smaller voltage spike that could be due to their good conductivity, which could promote the reactivity of the nonconductive active materials on the interface.

Fig. 4e represents the cycling stability of pristine, CC, GPN–PANI@CC Mg–S cells at a 0.1C rate, respectively. A capacity of 877 mA h g^{-1} was measured in the initial cycle of a pristine cell whereas, in the case of CC, GPN–PANI@CC cells a capacity value of 968 and 1121 mA h g^{-1} was determined, respectively. The high initial capacity of CC, GPN–PANI@CC could be mainly ascribed to the good electronic conductivity and the adsorption property of the interlayers. Further, the reversible capacity of pristine, CC and GPN–PANI@CC cells after 150 cycles was measured to be approximately 205, 305, and 500 mA h g^{-1}, respectively. The poor capacity retention of the pristine cell could be due to the dissolution and diffusion of higher-order polysulfide through the separator to the anode compartment. Whereas, the CC interlayer cell shows partial capacity degradation might be attributed to the limited polysulfide absorption capability of the CC interlayer. Compared to other cells, the cell with the GPN–PANI@CC interlayer showed superior electrochemical performance in terms of good capacity retention, high cycling stability and coulombic efficiency (Fig. 4d and f). This can be ascribed to the synergistic effects of the GPN–PANI composite, *i.e.* (i) the GPN host has high conductivity and surface area, which can enhance the reactivity of nonconductive sulfur material and improve the electrochemical kinetics; (ii) the conductive PANI with the polar amine and imine groups can chemically anchor the sulfur species and facilitate the sulfur redox kinetics.[60,61] In addition to this 60% sulfur loaded cell, other sulfur loading 70%, 80% cells are also studied (Fig. S11†). It is observed that as the sulfur loading increases the stability of the cells decreases. For comparison the GPN@CC, PANI@CC cells are also studied Fig. S12.† The GPN@CC cell shows initial higher capacities but due to the poor sulfophilic nature capacity degradation is also higher whereas PANI@CC cells show lower capacities with comparably good capacity retention due to the high abundant functional groups present on it. In addition to this, the electrochemical performance of the GPN–PANI composite cathode (without sulfur) *vs.* Mg anode, cells are also evaluated in similar electrolyte (0.4 M $Mg[B(hfip)_4]_2$/DME), mass loading (1 mg cm^{-2}), and voltage window (0.5–2.5 V). Corresponding electrochemical data along with charge–discharge profile are shown Fig. S13.† It is observed that the capacity contribution from the carbon is minimum (~20 mA h g^{-1}). Table S2† shows the electrochemical advantages of the GPN–PANI@CC interlayer cell over previously published Mg–S cells. The postmortem analysis of cycled cell is carried out inside the argon-filled glove box. Fig. S14 and S15† shows the SEM and elemental mapping analysis of the corresponding cathode and separator.

The polysulfide trapping ability of the GPN–PANI@CC interlayer can be visually examined by placing it into the 0.1 M Mg_xS_y/DME solution Fig. 5. Compared with the blank Mg_xS_y solution, the GPN–PANI@CC interlayer containing solution became colorless transparent within 12 h of aging. This demonstrates that the GPN–PANI@CC interlayer can effectively adsorb the Mg_xS_y species. To further understand the effect of the GPN–PANI composite interlayer, cross-section SEM of the GPN–PANI@CC interlayer containing Mg_xS_y/DME solution after

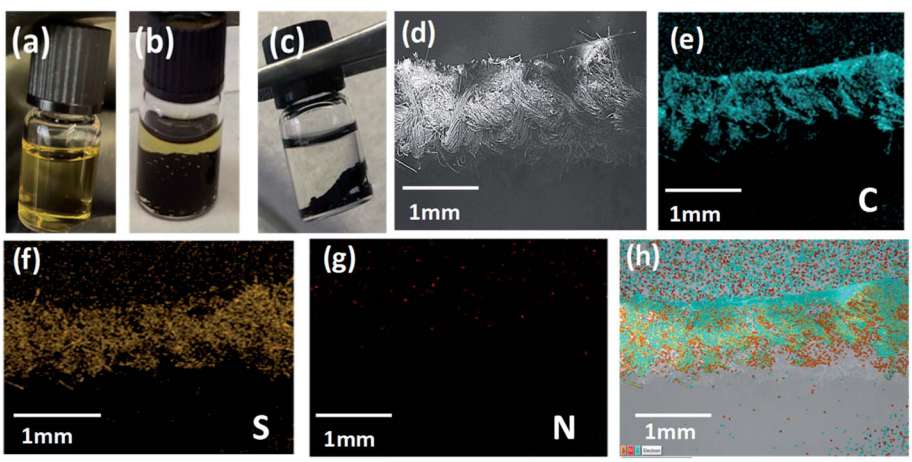

Fig. 5 Visual polysulfide adsorption test. Digital image of (a) 0.1 M Mg_xS_y/DME (b) Mg_xS_y with GPN PANI@CC interlayer (c) after aging for 12 h of Mg_xS_y/DME with GPN PANI@CC interlayer. (d) The cross section SEM of GPN PANI@CC interlayer after aging for 12 h in Mg_xS_y/DME (e h) elemental mapping of GPN PANI@CC interlayer.

12 h of aging is carried out (Fig. 5d–h). This shows the polysulfides and nitrogen are distributed evenly throughout the CC interlayer. This further confirms the polysulfides are adsorbed on the interlayer.

The advantages of the interlayer have also been studied in the $Mg(TFSI)_2$–$MgCl_2$ electrolyte. Here the similar cell configurations with the same cathode, anode, and interlayer were implemented. Unlike the MBR electrolyte, the $Mg(TFSI)_2$–$MgCl_2$ electrolyte is not stable at a voltage higher than 2.4 V,[31] so the charge–discharge voltage window was set in the range of 0.3–2.4 V. Fig. 6a, c and e shows the galvanostatic charge–discharge cycling curves of pristine, CC, GPN–PANI@CC interlayer cells at 0.1C. The charge–discharge profiles exhibit different features with these two electrolytes. In the case of MBR, the voltage plateau at ~1.5 V was relatively flat whereas it was sloping in $Mg(TFSI)_2$–$MgCl_2$ electrolyte. In the pristine cell with the $Mg(TFSI)_2$–$MgCl_2$ electrolyte, the high-order polysulfide region was not observed (above 1.4 V) and poor capacity values were measured Fig. 6b.

Though interlayer cells (Fig. 6d and f) showed relatively stable cycling behavior, the coulombic efficiency was rather unstable, implying the severe degradation of the electrolyte. In comparison, the GPN–PANI@CC interlayer cells could demonstrate relatively good capacity retention, delivering a capacity of approximately 380 mA h g^{-1} after 150 cycles. Nevertheless, their electrochemical performance was inferior to that of the cells with the borate MBR electrolytes.

Fig. S16† shows the comparison of the charge–discharge profiles of the GPN–PANI@CC interlayer cells in MBR electrolyte and $Mg(TFSI)_2$–$MgCl_2$ electrolyte in the first and 30th cycle, respectively. Both cells exhibited a nearly similar overpotential in the initial cycle; however, upon cycling, the ΔE dramatically increased in the electrolyte cells. These differences indicate that high cell resistance can be created in the $Mg(TFSI)_2$–$MgCl_2$ electrolyte, which could be caused by the $Mg(TFSI)_2$ salt decomposition.[62 64] Hence, the MBR electrolyte along with the GPN–PANI@CC interlayer is more favorable for improving the Mg–S battery performance.

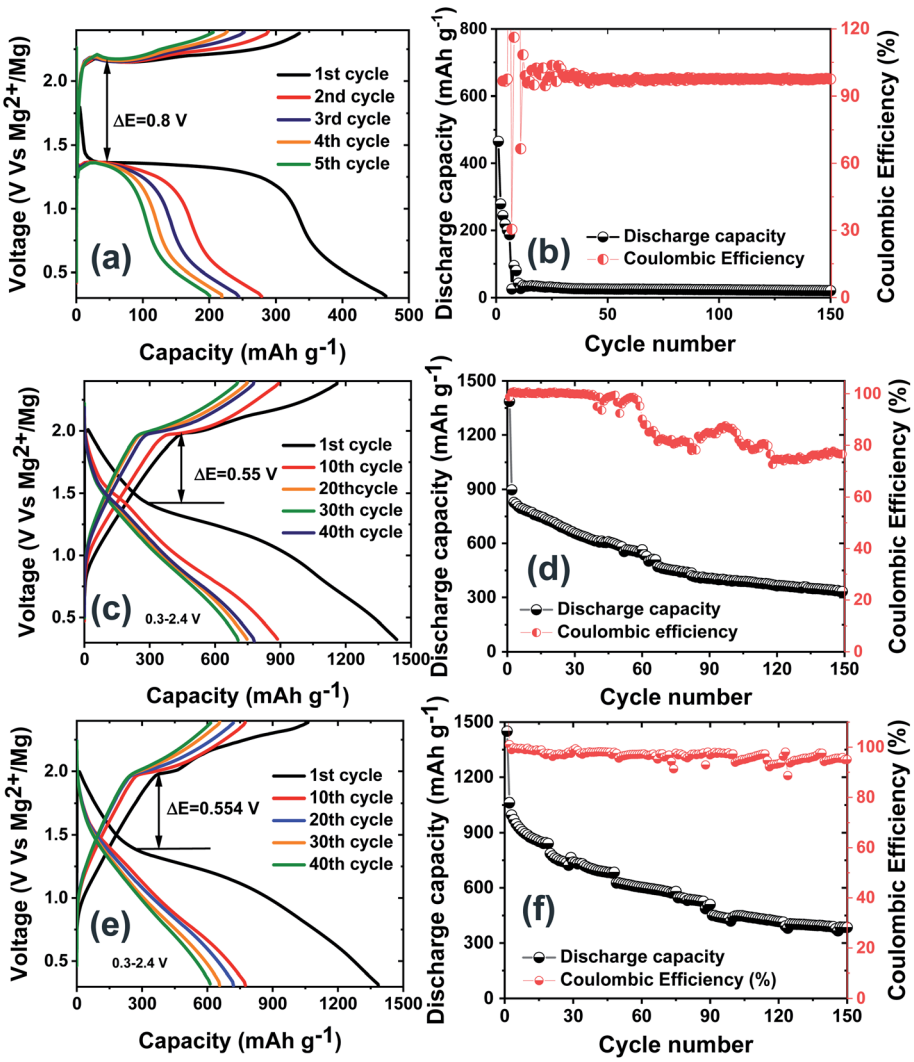

Fig. 6 The electrochemical behavior of the pristine, CC, GPN PANI@CC interlayer cells in $Mg(TFSI)_2$ $MgCl_2$ electrolyte (a, c and e) charge discharge cycling curves of (b, d and f) capacity and coulombic efficiency *vs.* cycle number plot.

Conclusions

In summary, the self-discharge behavior of the Mg–S cells in MBR and $Mg(TFSI)_2$–$MgCl_2$ electrolytes have been investigated. The spontaneous formation of various magnesium polysulfides in the mixture of sulfur and Mg in both electrolyte solutions have been visualized, which can be identified as the cause for self-discharge in Mg–S cells. In the self-discharge tests, the pristine cell underwent severe polysulfide dissolution in the OCV period. The interlayer strategy has been employed for polysulfide mitigation. Among them, the GPN–PANI@CC interlayer can effectively control the polysulfide diffusion of the Mg–S cells due to its chemical functionality for immobilizing sulfur species and high electron conductivity for facilitating the sulfur redox kinetics. Further, the electrochemical behavior of these cells was studied both in MBR and $Mg(TFSI)_2$–$MgCl_2$ electrolytes. The GPN–PANI@CC interlayer cell in MBR electrolyte showed superior performance in terms of low self-discharge, good capacity retention and coulombic efficiency over 150 cycles.

Conflicts of interest

The authors declare no conflict of interest.

Acknowledgements

This work was supported by the Federal Ministry of Education and Research (Bundesministerium für Bildung und Forschung, BMBF) of Germany within the project "MagSiMal" (03XP0208). This work contributes to the research performed at CELEST (Center for Electrochemical Energy Storage Ulm-Karlsruhe). The authors thank Deutsche Forschungsgemeinschaft (DFG, German Research Foundation) under Germanys Excellence Strategy EXC 2154, project number 390874152.

References

1 E. M. Erickson, E. Markevich, G. Salitra, D. Sharon, D. Hirshberg, E. de la Llave, I. Shterenberg, A. Rosenman, A. Frimer and D. Aurbach, *J. Electrochem. Soc.*, 2015, **162**, A2424–A2438.

2 Y. Miao, P. Hynan, A. von Jouanne and A. Yokochi, *Energ.*, 2019, **12**, 1074.

3 M. Salama, Rosy, R. Attias, R. Yemini, Y. Gofer, D. Aurbach and M. Noked, *ACS Energy Lett.*, 2019, **4**, 436.

4 S.-H. Chung and A. Manthiram, *Adv. Mater.*, 2019, **31**, 1901125.

5 X. Yu and A. Manthiram, *Adv. Funct. Mater.*, 2020, **30**, 2004084.

6 Z. Li, B. P. Vinayan, T. Diemant, R. J. Behm, M. Fichtner and Z. Zhao-Karger, *Small*, 2020, **16**, 2070216.

7 A. Scafuri, R. Berthelot, K. Pirnat, A. Vizintin, J. Bitenc, G. Aquilanti, D. Foix, R. Dedryvère, I. Arčon, R. Dominko and L. Stievano, *Chem. Mater.*, 2020, **32**, 8266–8275.

8 T. Gao, X. Li, X. Wang, J. Hu, F. Han, X. Fan, L. Suo, A. J. Pearse, S. B. Lee, G. W. Rubloff, K. J. Gaskell, M. Noked and C. Wang, *Angew. Chem., Int. Ed.*, 2016, **55**, 9898–9901.

9 A. Ponrouch, J. Bitenc, R. Dominko, N. Lindahl, P. Johansson and M. R. Palacin, *Energy Storage Mater.*, 2019, **20**, 253–262.

10 A. Gnanavel, D. Bosubabu, K. Ramesha and V. Rangarajan, *J. Electroanal. Chem.*, 2019, **843**, 37–46.

11 D. Bosubabu, J. Sivaraj, P. Gurunathan and K. Ramesha, *Energy Fuels*, 2020, **34**, 16810–16818.

12 J. Sun, C. Deng, Y. Bi, K.-H. Wu, S. Zhu, Z. Xie, C. Li, R. Amal, J. Luo, T. Liu and D.-W. Wang, *ACS Appl. Energy Mater.*, 2020, **3**, 2516–2525.

13 R. Mohtadi and F. Mizuno, *Beilstein J. Nanotechnol.*, 2014, **5**, 1291–1311.

14 F. Bella, S. De Luca, L. Fagiolari, D. Versaci, J. Amici, C. Francia and S. Bodoardo, *Nanomaterials*, 2021, **11**, 810.

15 A. Ponrouch and M. R. Palacin, *Philos. Trans. R. Soc., A*, 2019, **377**, 20180297.

16 Z. Guo, S. Zhao, T. Li, D. Su, S. Guo and G. Wang, *Adv. Energy Mater.*, 2020, **10**, 1903591.

17 M. Rashad, M. Asif and Z. Ali, *Coord. Chem. Rev.*, 2020, **415**, 213312.

18 Z.-K. Zhirong and F. Maximilian, *MRS Commun.*, 2017, **7**, 770–784.

19 P. Wang and M. R. Buchmeiser, *Adv. Funct. Mater.*, 2019, **29**, 1905248.

20 J. Bitenc and R. Dominko, *Front. Chem.*, 2018, **6**, 634.

21 D. Bosubabu, J. Sivaraj, R. Sampathkumar and K. Ramesha, *ACS Appl. Energy Mater.*, 2019, **2**, 4118–4125.

22 Z. Zhao-Karger, X. Zhao, O. Fuhr and M. Fichtner, *RSC Adv.*, 2013, **3**, 16330–16335.

23 Z. Zhao-Karger and M. Fichtner, *Front. Chem.*, 2019, **6**, 1–12.

24 Z. Zhang, Z. Cui, L. Qiao, J. Guan, H. Xu, X. Wang, P. Hu, H. Du, S. Li, X. Zhou, S. Dong, Z. Liu, G. Cui and L. Chen, *Adv. Energy Mater.*, 2017, **7**, 1.

25 Y. Zhang, J. Xie, Y. Han and C. Li, *Adv. Mater.*, 2018, **30**, 1704166.

26 Y. Zhang, J. Xie, Y. Han and C. Li, *Adv. Funct. Mater.*, 2015, **25**, 7300–7308.

27 Z. Zhao-Karger, X. Zhao, O. Fuhr and M. Fichtner, *RSC Adv.*, 2013, **3**, 16330.

28 Z. Zhao-Karger, X. Zhao, D. Wang, T. Diemant, R. J. Behm and M. Fichtner, *Adv. Energy Mater.*, 2015, **5**, 1401155.

29 L. C. Merrill and J. L. Schaefer, *Langmuir*, 2017, **33**, 9426–9433.

30 B. P. Vinayan, Z. Zhao-Karger, T. Diemant, V. S. Chakravadhanula, N. I. Schwarzburger, M. A. Cambaz, R. J. Behm, C. Kubel and M. Fichtner, *Nanoscale*, 2016, **8**, 3296–3306.

31 T. Gao, S. Hou, F. Wang, Z. Ma, X. Li, K. Xu and C. Wang, *Angew. Chem., Int. Ed.*, 2017, **56**, 13526–13530.

32 D. Bosubabu and K. Ramesha, *Electrochim. Acta*, 2016, **219**, 295–304.

33 P. M. Ette, D. Bosubabu, M. L. Roy and K. Ramesha, *J. Power Sources*, 2019, **436**, 226850.

34 D. Bosubabu, R. N. Ramesha, P. M. Ette, A. K. N. Kumar, A. Arulraj and K. Ramesha, *J. Power Sources*, 2019, **436**, 226870.

35 D. Bosubabu, V. Parthiban, A. K. Sahu and K. Ramesha, *Bull. Mater. Sci.*, 2021, **44**, 1–7.

36 R. Mohtadi, O. Tutusaus, T. S. Arthur, Z. Zhao-Karger and M. Fichtner, *Joule*, 2021, **5**, 581–617.

37 D.-T. Nguyen, R. Horia, A. Y. S. Eng, S.-W. Song and Z. W. Seh, *Mater. Horiz.*, 2021, **8**, 830–853.

38 Z. Zhao-Karger, M. E. Gil Bardaji, O. Fuhr and M. Fichtner, *J. Mater. Chem. A*, 2017, **5**, 10815–10820.

39 Z. Zhao-Karger, R. Liu, W. Dai, Z. Li, T. Diemant, B. P. Vinayan, C. Bonatto Minella, X. Yu, A. Manthiram, R. J. Behm, M. Ruben and M. Fichtner, *ACS Energy Lett.*, 2018, **3**, 2005–2013.

40 B. P. Vinayan, H. Euchner, Z. Zhao-Karger, M. A. Cambaz, Z. Li, T. Diemant, R. J. Behm, A. Gross and M. Fichtner, *J. Mater. Chem. A*, 2019, **7**, 25490–25502.

41 J. Häcker, C. Danner, B. Sievert, I. Biswas, Z. Zhao-Karger, N. Wagner and K. A. Friedrich, *Electrochim. Acta*, 2020, **338**, 135787.

42 R. Richter, J. Häcker, Z. Zhao-Karger, T. Danner, N. Wagner, M. Fichtner, K. A. Friedrich and A. Latz, *ACS Appl. Energy Mater.*, 2020, **3**, 8457–8474.

43 H. O. Ford, E. S. Doyle, P. He, W. C. Boggess, A. G. Oliver, T. Wu, G. E. Sterbinsky and J. L. Schaefer, *Energy Environ. Sci.*, 2021, **14**, 890–899.

44 M. Jiang, B. Gan, Y. Deng, Y. Xiong and R. Tan, *Materials*, 2018, **12**, 64.

45 S. H. Chung, P. Han and A. Manthiram, *ACS Appl. Mater. Interfaces*, 2017, **9**, 20318–20323.

46 L. Wang, Y.-B. He, L. Shen, D. Lei, J. Ma, H. Ye, K. Shi, B. Li and F. Kang, *Nano Energy*, 2018, **50**, 367–375.

47 J. Q. Huang, T. Z. Zhuang, Q. Zhang, H. J. Peng, C. M. Chen and F. Wei, *ACS Nano*, 2015, **9**, 3002–3011.

48 D. B. Babu and K. Ramesha, *Carbon*, 2019, **144**, 582–590.

49 Y. Ji, X. Liu-Théato, Y. Xiu, S. Indris, C. Njel, J. Maibach, H. Ehrenberg, M. Fichtner and Z. Zhao-Karger, *Adv. Funct. Mater.*, 2021, **31**, 2100868.

50 H. Kaland, F. Haskjold Fagerli, J. Hadler-Jacobsen, Z. Zhao-Karger, M. Fichtner, K. Wiik and N. P. Wagner, *ChemSusChem*, 2021, **14**, 1864–1873.

51 D. Bosubabu, R. Sampathkumar, G. Karkera and K. Ramesha, *Energy Fuels*, 2021, **35**, 8286–8294.

52 D. Bosubabu, J. Sivaraj, P. Gurunathan and K. Ramesha, *Energy Fuels*, 2020, **34**, 16810–16818.

53 D. B. Babu, K. Giribabu and K. Ramesha, *ACS Appl. Mater. Interfaces*, 2018, **10**, 19721–19729.

54 G. Angamuthu, D. Bosubabu, K. Ramesha and V. Rengarajan, *Appl. Mater. Today.*, 2021, **22**, 100916.

55 D. B. Babu, R. N. Ramesha, P. M. Ette, A. K. Nanda Kumar, A. Arulraj and K. Ramesha, *J. Power Sources*, 2019, **436**, 226870.

56 Y. Xu, Y. Ye, S. Zhao, J. Feng, J. Li, H. Chen, A. Yang, F. Shi, L. Jia, Y. Wu, X. Yu, P. A. Glans-Suzuki, Y. Cui, J. Guo and Y. Zhang, *Nano Lett.*, 2019, **19**, 2928–2934.

57 D. Zheng, X. Zhang, C. Li, M. E. McKinnon, R. G. Sadok, D. Qu, X. Yu, H.-S. Lee, X.-Q. Yang and D. Qu, *J. Electrochem. Soc.*, 2014, **162**, A203–A206.

58 G. Bieker, J. Wellmann, M. Kolek, K. Jalkanen, M. Winter and P. Bieker, *Phys. Chem. Chem. Phys.*, 2017, **19**, 11152–11162.

59 S. Drvarič Talian, A. Vizintin, J. Bitenc, G. Aquilanti, A. Randon-Vitanova, M. Gaberšček and R. Dominko, *ChemElectroChem*, 2021, **8**, 1062–1069.

60 C. Y. Chen, H. J. Peng, T. Z. Hou, P. Y. Zhai, B. Q. Li, C. Tang, W. Zhu, J. Q. Huang and Q. Zhang, *Adv. Mater.*, 2017, **29**, 1606802.

61 X. Hong, Y. Liu, Y. Li, X. Wang, J. Fu and X. Wang, *Polymers*, 2020, **12**, 331.

62 M. S. Ding, T. Diemant, R. J. Behm, S. Passerini and G. A. Giffin, *J. Electrochem. Soc.*, 2018, **165**, A1983–A1990.

63 S.-J. Kang, H. Kim, S. Hwang, M. Jo, M. Jang, C. Park, S.-T. Hong and H. Lee, *ACS Appl. Mater. Interfaces*, 2019, **11**, 517–524.

64 X. Li, T. Gao, F. Han, Z. Ma, X. Fan, S. Hou, N. Eidson, W. Li and C. Wang, *Adv. Energy Mater.*, 2018, **8**, 1.